

Viscous flow past a flexible fiber tethered at its center point: vortex shedding

Luoding Zhu

Dept of Mathematical Sciences

Indiana University-Purdue University Indianapolis

Indianapolis, Indiana, USA

lzhu@math.iupui.edu

Abstract

Motivated by a laboratory experiment reported in Alben, Shelley & Zhang (2002) (*Nature* **420**, 479), we performed simulations of an elastic fiber anchored at the center point immersed in a flowing viscous incompressible fluid by the immersed boundary (IB) method. We focused on the influence of some dimensionless parameters on vortex shedding from the fiber for Re in the range of $[30, 800]$. Three sets of simulations were designed to investigate the influence of Reynolds number Re , dimensionless fiber flexure modulus \hat{K}_b , and dimensionless fiber length \hat{L} on vortex shedding. According to the simulation results, Re , \hat{K}_b , and \hat{L} each has significant influence on the structure of shed vortices. However, Re has little influence on the vortex shedding frequency. With the increase of dimensionless bending modulus, the dimensionless vortex shedding frequency (f_{vs}) and the critical Reynolds number (Re_c) decrease approximately as power law functions. Both f_{vs} and Re_c increase approximately linearly as dimensionless fiber length increases.

I. Introduction

Vortex shedding from an object immersed in a flowing fluid is an important and interesting topic and has been extensively studied experimentally, analytically and computationally (Sarpkaya 1979; Griffin 1982; Bearman 1989; Parkinson 1989; Williamson 2004). Most of the work has focused on vortex shedding from a rigid body. For instance, vortex shedding from a circular cylinder (tube) was studied by Abarbane et al. (1991), Nitsche & Krasny (1994), and Wang & Zhou (2004); from a sphere was studied by Lee (2000); from an (inclined) flat plate was studied by Sarpkaya (1975) and Krasny (1990). Recently, Zhu & Peskin (2002,2003) studied numerically the vortex shedding from elastic flapping filaments interacting with a flowing viscous fluid. Very recently Jung et al. (2006) studied experimentally the vortex shedding from a flexible flapping rubber loop in a flowing soap film. Here we report our simulation of vortex shedding from a flexible fiber with its center point tethered (otherwise unrestricted) in a two-dimensional flowing viscous incompressible fluid by the immersed boundary (IB) method (Peskin 1977; Peskin 1996; Peskin 2002; Zhu & Peskin 2002).

The direct motivation of our work is a laboratory experiment reported in Alben et al. (2002, 2004) and Alben (2004). The experiment used a flowing soap film (thickness $1 - 3 \mu m$) as a flow tunnel. A flexible glass fiber (diameter $34 \mu m$) was introduced with its middle point anchored at the center of the flow channel and nowhere else constrained. The Reynolds number ranged from 2000 to 40,000 in the experiment. Alben et al. investigated the drag reduction induced by self-similar bending and streamlining of the fiber (Alben et al. 2002, 2004). Very recently, Zhu & Peskin (2007) computed the averaged drag of an elastic fiber immersed in a 2D flowing incompressible viscous fluid at intermediate Reynolds numbers. One of our results was that when the inflow speed was sufficiently high, the flow became unsteady. Vortex shedding

from the fiber became evident, the fiber vibrated and the drag-coefficient versus time ($C_d - t$) curve oscillated.

Our current work investigates the influence of some dimensionless flow parameters on the vortex shedding. In our work, the flowing soap film was modelled by a 2D viscous incompressible laminar channel flow, and the flexible fiber was simulated by a one-dimensional linear elastic curve. The fiber was assumed to be totally immersed and neutrally buoyant in the flowing fluid. The mathematical formulation and numerical method were based on the FFT version of the IB method (Peskin 1996; Peskin 2002; Zhu 2001). Our work investigates the vortex shedding at lower Reynolds numbers (30 – 800), focusing on the influence of the Reynolds number (Re), dimensionless fiber flexure modulus (\hat{K}_b), and dimensionless fiber length (\hat{L}) on the vortex shedding.

II. Governing Equations

Using standard notation (\mathbf{u} for velocity, ρ for mass density, p for pressure, \mathbf{x} for Eulerian spatial coordinates, t for time, and α for the Lagrangian coordinate that was chosen as the fiber arc-length at the initial configuration and was frozen throughout a simulation), the equations governing the motion of both the fluid and the fiber (neutrally buoyant) in dimensionless form read as follows (the IB formulation):

$$\frac{D\mathbf{u}(\mathbf{x}, t)}{Dt} + \nabla p(\mathbf{x}, t) = \frac{1}{Re} \Delta \mathbf{u}(\mathbf{x}, t) + \mathbf{f}(\mathbf{x}, t) - Fr^{-1} \mathbf{u}(\mathbf{x}, t) - \mathbf{g} \quad (1)$$

$$\nabla \cdot \mathbf{u}(\mathbf{x}, t) = 0 \quad (2)$$

$$\mathbf{f}(\mathbf{x}, t) = \int \mathbf{F}(\alpha, t) \delta(\mathbf{x} - \mathbf{X}(\alpha, t)) d\alpha \quad (3)$$

$$\mathbf{F}(\alpha, t) = -\frac{\partial e}{\partial \mathbf{X}} = -\frac{\partial(e_s + e_b)}{\partial \mathbf{X}} \quad (4)$$

$$e_s = \frac{1}{2L} \hat{K}_s \int (|\frac{\partial \mathbf{X}(\alpha, t)}{\partial \alpha}| - 1)^2 d\alpha \quad (5)$$

$$e_b = \frac{1}{2L} \hat{K}_b \int |\frac{\partial^2 \mathbf{X}(\alpha, t)}{\partial \alpha^2}|^2 d\alpha \quad (6)$$

$$\frac{\partial \mathbf{X}}{\partial t}(\alpha, t) = \mathbf{U}(\alpha, t) \quad (7)$$

$$\mathbf{U}(\alpha, t) = \int \mathbf{u}(\mathbf{x}, t) \delta(\mathbf{x} - \mathbf{X}(\alpha, t)) d\mathbf{x} \quad (8)$$

Here $\frac{D}{Dt} = \frac{\partial}{\partial t} + \mathbf{u} \cdot \frac{\partial}{\partial \mathbf{x}}$ is the material derivative, the vector $\mathbf{g} = (0, Fr^{-1})^T$ and Fr is the Froude number. Re is the Reynolds number, e is the fiber elastic potential energy density, and e_s and e_b are fiber elastic energy density associated with compression/stretching and bending, respectively. \hat{K}_s is the dimensionless stretching/compression coefficient, \hat{K}_b is the dimensionless flexure modulus, and L is the fiber total length. See Table 2 for definitions of these non-dimensional quantities and their values used in the simulations.

Eqs. (1-2) are the incompressible viscous Navier-Stokes equations governing the motions of both the fluid and the fiber. The term $-Fr^{-1}\mathbf{u}$ is the air resistance where the coefficient

happens to be the reciprocal of Froude number. (The dimensional air resistance coefficient, λ , was determined by the equation $\lambda|V_0| = \rho_0 g$. Here V_0 is the inflow speed, ρ_0 is the fluid mass density¹, and g is the gravitational acceleration constant. If ρ_0, V_0 and L are chosen as reference quantities to nondimensionalize the IB formulation, the air resistance term $-\lambda \mathbf{u}$ becomes $-g^* \mathbf{u}^*$, where the quantities with a “*” denote their corresponding dimensionless equivalent. It turns out that the g^* equals to Fr^{-1} in our case.) Eqn. (7) updates the position and shape of the fiber. The fiber velocity $\mathbf{U}(\alpha, t)$ is interpolated by Eqn. (8) from the velocity of the fluid. From the fiber configuration $\mathbf{X}(\alpha, t)$ the elastic potential energy density (e) is calculated via Eqs. (5-6) and the Lagrangian force density $\mathbf{F}(\alpha, t)$ is computed through Eqn.(4). The immersed boundary force $\mathbf{f}(\mathbf{x}, t)$ on the right hand side of Eqn. (1) is reckoned using Eqn. (3). Eqs (1-8) constitute a nonlinear system of integral-differential equations which depicts the motions of the viscous fluid and the elastic fiber. The system is completed by imposing proper initial and boundary conditions. The initial velocity was the steady solution to the 2D stationary channel flow under the action of gravity and air resistance in the absence of the fiber. See Fig. 1 for a typical initial velocity profile. The initial velocity profile was imposed on the inlet and outlet. The velocity was zero on the two side boundaries. The fiber middle point ($\mathbf{X}(s_c, t)$, where s_c is the Lagrangian coordinate for the middle point) was tethered at a fixed Eulerian point (x_0, y_0) by a virtual spring with the same stiffness as the inextensible fiber itself. It was found that $\mathbf{X}(s_c, t)$ was almost constant in all simulations.

III. Simulation Results

The above nonlinear system of integral-differential equations was discretized on a non-

¹The difference between ρ and ρ_0 is as follow: ρ is the mass density of the fluid-fiber system, ρ_0 is the mass density of the fluid. For a neutrally buoyant immersed structure as in our case, $\rho = \rho_0$.

staggered uniform fixed Eulerian grid. The backward Euler method was used for time derivatives and the center differencing was used for spatial derivatives (both gradient and divergence operators). The skew-symmetrical scheme was used for the convection term and the nonlinearity therein was removed by using the velocity at the previous time step. The immersed boundary force \mathbf{f} was treated explicitly. The resultant linear algebraic system with constant coefficients was solved by the Discrete Fast Fourier Transform (DFFT). The dimensionless time-step size was $\Delta t = 10^{-4}$. The spatial grid size was 256×512 . See Peskin (1996) and Zhu (2001) for the details of discretization and how the algebraic system was solved by the DFFT.

The parameters (dimensional) used in our simulations are tabulated in Table 1. Some parameters remained fixed throughout all the simulations reported here, and their values (as in Table 1) will not be stated again for each simulation reported below. These included fluid density (ρ_0), gravitational acceleration constant (g), compression/stretching coefficient K_s , and height (H) of the computational domain.

In our simulations we used the values of all the dimensional parameters in the laboratory experiment except the fluid viscosity and the channel width. The viscosity is approximately 100 times greater than in the experiment which causes the Reynolds numbers in our simulations to be smaller by approximately two orders of magnitude. The channel width was fixed to be 9 cm in the experiment. In the simulations to investigate the influence of dimensionless fiber length, the channel width was varied from 9 cm to 2 cm. (Note that varying the fiber length causes changes not only in \hat{L} , but also in Re and \hat{K}_b . See table 2.) For all other simulations in this paper, the channel width was fixed to be 9 cm (the experimental value). The values of all the other dimensional and dimensionless parameters are within the experimental ranges.

In addition to the Reynolds (Re) and Froude numbers (Fr), our elastic-fiber-fluid problem

(fiber neutrally buoyant in fluid) has a few other non-dimensional parameters. They are the dimensionless fiber flexure modulus (\hat{K}_b), dimensionless fiber length (\hat{L}), and the dimensionless compression/stretching coefficient (\hat{K}_s). See Table 2 for their definitions and values used in our simulations. In general it is expected that the vortex shedding and drag-coefficient is an outcome of the interplay of these dimensionless quantities.

The fiber physical compression/stretching coefficient K_s was chosen such that the fiber was almost inextensible in all simulations: the relative increase and decrease in fiber length was less than 0.25%. Even though \hat{K}_s varied with V_0 and L , we assumed that the influence of \hat{K}_s on the fluid-fiber problem was not important because it was very large in each case. The fiber mass density has been found to play no important role in the fiber drag-coefficient (Zhu & Peskin 2007). Therefore the fiber was assumed to be neutrally buoyant in the fluid. Also no significant influence of the Froude number Fr on the vortex shedding and fiber drag was expected. Therefore, the influence of \hat{K}_s and Fr on vortex shedding shall not be discussed, and only those of Reynolds number, dimensionless flexure modulus and dimensionless fiber length will be addressed explicitly.

To isolate the effect of Reynolds number, a series of simulations with varying fluid kinematic viscosity were performed. Note that only the Reynolds number varied from simulation to simulation throughout the series. All the other dimensionless parameters were constant. An analogous series of simulations were performed to single out the influence of the dimensionless flexure modulus. In this series only the dimensional flexure modulus (K_b) varied. Therefore only \hat{K}_b varied throughout this series of simulations. The third series of simulations were run to show the influence of the dimensionless fiber length, with only the channel width W being varied in this series.

inflow speed (V_0)	50 – 300 <i>cm/sec</i>
fluid kinematic viscosity (ν)	1 – 22 <i>cm²/sec</i>
fluid density (ρ_0)	3×10^{-4} <i>g/cm²</i>
fiber length (L)	1 – 5 <i>cm</i>
fiber flexure modulus (K_b)	$0.28 - 10^3$ <i>erg · cm</i>
compression/stretching coeff (K_s)	2.4×10^6 <i>dyn/cm</i>
gravitational acceleration (g)	980 <i>cm/sec²</i>
width of the film (W)	2.0 – 9.0 <i>cm</i>
height of the film (H)	18 <i>cm</i>

Table 1: Parameters used in the simulations

Name	Definition	Range
Reynolds Number (Re)	$\frac{V_0 L}{\nu}$	30 – 800
Froude Number (Fr)	$\frac{V_0^2}{gL}$	3.09 – 91.84
Filament Length (\hat{L})	$\frac{L}{W}$	0.11 – 0.8
Dimensionless Flexure Modulus (\hat{K}_b)	$\frac{K_b}{\rho_0 V_0^2 L^3}$	$2.89 \times 10^{-4} - 0.1037$
Dimensionless Stretching Coeff (\hat{K}_s)	$\frac{K_s}{\rho_0 V_0^2 L}$	$1.8 \times 10^4 - 1.25 \times 10^7$

Table 2: Non-dimensional parameters used in the simulations. For the meanings of the symbols used in the definition of the non-dimensional parameters, see Table 1.

The instantaneous drag (D) the fiber experiences is computed the same way as in Zhu & Peskin (2007). The drag-coefficient is defined as $C_d = \frac{D}{\frac{1}{2}\rho_0 V_0^2 L}$. A time-averaged drag-coefficient \bar{C}_d is defined as $\bar{C}_d = \frac{\bar{D}}{\frac{1}{2}\rho_0 V_0^2 L}$. Here \bar{D} is the time-averaged drag which is computed over N equally spaced instants between time T_{qs} and T_e . Here T_{qs} is some time after the initial transition dies out and the fiber reaches a small-amplitude oscillation state (“quasi-steady” state for shorthand). $T_{qs} = 10$ for this work. The simulation terminal time T_e and the time spacing between two neighboring instantaneous drag computations T_s are chosen arbitrarily. In this work $T_s = 0.05$, and $T_e = 24 - 30$.

The remainder of this section is structured as follows. First the influence of Re on vortex shedding and drag-coefficient is discussed. Then follows the influence of \hat{K}_b . The third part addresses the influence of the dimensionless fiber length.

1. Influence of Reynolds number

To investigate the influence of Re , a series of simulations with different kinematic viscosity ν were performed. The fluid kinematic viscosity ν ranged from 1 to 22 (cm^2/s). The corresponding Re ranged from 30 to 800. The other parameters used in this series of simulations were as follows: $L = 3.3$ cm, $V_0 = 200$ cm/s, $K_b = 2.8$ erg · cm. The values of dimensionless parameters were: $\hat{K}_b = 6.5 \times 10^{-3}$, $\hat{L} = 0.37$, $Fr = 12.37$, $\hat{K}_s = 6.1 \times 10^4$. Four typical simulation results are shown in Fig. 2. In this figure, the top panel plots the instantaneous positions of fluid markers² (used to visualize the fluid motion) at time $T = 24$ (dimensionless), and the lower panel plots the corresponding vorticity contours (for visualization of the vortical field) at the same time instant. These four typical simulations show the influence of the Reynolds

²The markers were released on the inlet boundary periodically. They were massless and moved with the fluid. Their velocity was interpolated from that of the fluid exactly as the fiber velocity was computed.

number on vortex shedding. Vortex shedding is not observed when the Reynolds number $Re \leq 155$. When the Reynolds number is around 165, vortex shedding starts to show. With the increase of Re the vortex shedding becomes more apparent and intensive. The wake zone behind the fiber widens. The vortices shed become nearly perpendicular to the mainstream flow from being nearly aligned with the flow. (A shed vortex can be roughly approximated as an ellipse. The ellipse's long axis is used to determine whether the vortex is perpendicular to or aligned with the mainstream direction.) Fig. 3 demonstrates the influence of Re on the motion of the fiber and the drag-coefficient C_d for the above four typical simulations. The upper panel plots C_d versus time; the lower panel plots the fiber position and shape for the corresponding case. Dotted lines are used for $t \leq T_{qs}$ and solid lines for $t \geq T_{qs}$. The thickness of the solid dark line indicates the range of oscillation. The fiber vibrates within this range after T_{qs} . From Fig. 3 we can see that with the increase of Reynolds number, the opening of the parabola (fiber positions) widens and the fiber oscillation range increases (the dark line thickens). However, the drag-coefficient of the fiber seems to be quite insensitive to the Reynolds number within the range 200 – 800. The drag-coefficient-versus-time curves (C_d-t curves) look quite similar to each other (notice the curve for $Re = 82.5$ is slightly above the other three). One may expect the $C_d - t$ curve would become more oscillatory with the increase of Reynolds number as a consequence of intensified fiber vibration (probably induced by enhanced vortex shedding). But according to our simulations, this is not the case. The drag-coefficient C_d versus Re is given in Fig. 4 for Reynolds number in [30, 800]. It is seen that C_d is roughly a constant for Re between 200 and 800, but when Re gets smaller than approximately 200, the drag-coefficient begins to increase, first slightly and then rapidly. It seems that the increase of shape drag is well offset by the decrease of friction drag as Re

increases in the range (200, 800). When Re gets sufficiently small, the increase of friction drag comes to dominate and thus causes a significant increase in the drag-coefficient.

A critical Reynolds number Re_c for vortex shedding is defined as the Re at which the steady wake becomes unstable (sustained wake oscillation begins) after the initial transition period. It was found that Re_c varies with the dimensionless fiber modulus and length. It is 82 ± 5 by the method of bisection for the values of \hat{K}_b and \hat{L} used for this set of simulations. The vortex shedding frequency is not sensitive to Re in the range (160, 800) where vortex shedding is obvious. It is roughly a constant of 75. Nondimensionalized by $\frac{V_0}{L}$, the dimensionless vortex shedding frequency f_{vs} is approximately 1.2.

Based on the sequence of simulations with Re in [30, 800], we may conclude that while Reynolds number has significant influence on the structure of shed vortices, it has little influence on the vortex shedding frequency and the averaged drag-coefficient (\bar{C}_d) for Re in (200, 800).

2. Influence of dimensionless flexure modulus

A series of simulations with varying flexure modulus (\hat{K}_b) were performed to explore the influence of flexure modulus on the vortex shedding and drag-coefficient. All other parameters were kept the same. The value of \hat{K}_b varied from 0.1037 to 2.89×10^{-4} . The other dimensionless parameters were: $Re = 247.5$, $\hat{L} = 0.37$, $Fr = 27.83$, $\hat{K}_s = 2.69 \times 10^4$. The inflow speed was $V_0 = 300 \text{ cm/s}$, the fiber was 3.3 cm long. See Fig. 5 for four typical simulation results with different flexure modulus. From this figure we see that the flexure modulus has significant influence on the structure of shed vortices. As \hat{K}_b decreases, the fiber becomes more flexible. It bends and gets streamlined more easily. The wake behind the fiber narrows and the vortices shed look quite different. As \hat{K}_b decreases, the shed vortices are approximately aligned with

the mainstream flow at first, then become nearly perpendicular to the flow, and finally return to the state of being aligned with the flow. Fig. 6 plots the drag-coefficient versus time and the position of the fiber. As the flexure modulus decreases between 0.1037 and 1.44×10^{-3} fiber vibration becomes more violent. Consequently the $C_d - t$ curve becomes more oscillatory. When the flexure modulus is further decreased, the fiber becomes more aligned with the flow and less fiber oscillation is seen. Consequently the $C_d - t$ curve is less oscillatory. This may be explained as follows. To oscillate in this situation (the majority of the fiber is almost parallel to the mainstream flow), the fiber has to displace more fluid with larger momentum in the vertical direction (y -component of momentum). This restricts the motion of the fiber. Therefore, the fiber vibrates in a narrower range and the $C_d - t$ curve is less oscillatory. It is worth noticing that the drag-coefficient as a function of time monotonically decreases as the flexure modulus decreases as shown in the top panel of Fig. 6 (see Zhu & Peskin 2007) for a detailed $C_d - \hat{K}_b$ plot). This is probably because the shape drag dominates the total drag and apparently it becomes less and less when the fiber gets more and more aligned with the mainstream flow due to the decrease in flexure modulus.

Fig. 7 plots the dimensionless vortex shedding frequency f_{vs} versus dimensionless bending modulus \hat{K}_b . The top is a regular plot, the bottom is a log-log plot. The data on the log-log scale is best fitted by the line $y = -0.14x - 0.77$. This indicates that f_{vs} decreases as a power law function of \hat{K}_b in the range $(10^{-4}, 0.1)$, i.e. $f_{vs} \sim \hat{K}_b^{-0.14}$. This may be qualitatively explained as follows: the smaller the \hat{K}_b , the more flexible the fiber, as a consequence the fiber is more aligned with the mainstream flow, and thus the vortices formed and attached to the fiber get washed away more easily by the mainstream flow.

Fig. 8 plots on a log-log scale the critical Reynolds number for vortex shedding Re_c (defined

as in Section 1) as a function of dimensionless bending modulus \hat{K}_b . The data is best fitted by the line $y = -0.12x + 4.1$ in the least squares sense which indicates that the Re_c decreases approximately in a power law with \hat{K}_b in the range $(10^{-4}, 0.1)$, i.e., $Re_c \sim \hat{K}_b^{-0.12}$. Re_c is determined by the bisection method and has an error of ± 5 .

At first glance the above two results seem to be contradictory. One would expect that an increase of vortex shedding frequency as \hat{K}_b gets smaller would indicate vortex shedding becomes easier as \hat{K}_b decreases, and thus the critical Reynolds number should decrease as \hat{K}_b decreases. However this is not true according to our simulations. The reason is as follows: Re_c is defined as the minimum Reynolds number that causes sustained oscillation of the wake. As \hat{K}_b decreases the fiber becomes more aligned with the mainstream flow and represents a smaller and smoother obstacle to the flow. Therefore the wake becomes narrower and self-sustained oscillation becomes more difficult to occur (the narrower wake is constrained on both sides by widened mainstream flow with greater momentum along the y-direction).

Based on the sequence of simulations with \hat{K}_b in $[2.89 \times 10^{-4}, 0.1037]$, it may be concluded that the fiber dimensionless flexure modulus has significant influence on the vortex shedding, the fiber vibration, and the $C_d - t$ curve. When \hat{K}_b increases in the above range, both f_{vs} and Re_c decrease approximately as power laws in \hat{K}_b .

3. Influence of dimensionless fiber length

To study the influence of the dimensionless fiber length on vortex shedding, a group of simulations with different channel width W were performed. W ranged from 2 to 9 cm. All the other dimensional parameters were kept the same for all simulations in the group: $L = 1.6 \text{ cm}$, $V_0 = 200 \text{ cm/s}$, $\nu = 2.1333 \text{ cm}^2/\text{s}$, $K_b = 0.25 \text{ erg} \cdot \text{cm}$. The four typical cases are depicted in Fig. 9. The dimensionless fiber length \hat{L} for these four cases was 0.1778, 0.4, 0.6

and 0.8. The corresponding Reynolds number was 150, the dimensionless flexure modulus was 0.005086, the Fr was 25.51, and the \hat{K}_s was 1.25×10^7 .

Fig. 9 demonstrates that the \hat{L} has significant influence on vortex shedding. As \hat{L} increases in (0.17, 0.8), the number of shed vortices increases (i.e. shedding frequency increases). The shed vortices are detached from each other at the beginning, but become somewhat attached to each other as \hat{L} increases. The wake zone becomes narrower and the shed vortices directly interact with the boundary layers as they are carried away downstream.

Fig. 10 plots the drag-coefficient as a function of time and the position of the fiber at the “quasi-steady” state. With the increase of \hat{L} , the opening of the fiber contracts gradually and the fiber becomes more aligned with the flow (although \hat{K}_b was fixed). The height of the $C_d - t$ curve increases slightly with the increase of \hat{L} . The degree of oscillation in the $C_d - t$ curve is roughly the same. Fig. 11 plots the averaged drag-coefficient \bar{C}_d versus \hat{L} . It is interesting to notice that the averaged drag-coefficient (after T_{qs}) is an increasing function of the dimensionless fiber length. One may expect that as W decreases (i.e. \hat{L} increases), the fiber becomes more aligned and streamlined with the main flow, thus the drag should somehow decrease gradually in this case (notice Re is constant). However our simulation result suggests the opposite which may be explained as follows: as \hat{L} increases, the boundary layers on the channel entry portion (above the tethered point of the fiber) on the two side walls have almost the same thickness (see Fig. 9). Therefore the percentage of the boundary layers’ thickness with respect to the channel width increases, and the percentage of the channel width available to the freely flowing fluid (outside the boundary layers) decreases. Because the inlet flow speed is the same, the oncoming flow towards the fiber possesses a greater “effective speed” than the inlet speed. Hence the fiber experiences more drag as \hat{L} increases. This effect seems to reach

a maximum when \hat{L} reaches approximately 0.6. After that the $C_d - \hat{L}$ curve levels off. This explains as well why the fiber gets more aligned with the mainstream flow as \hat{L} increases, as shown in the bottom panel of Fig. 9.

Fig. 12 plots the dimensionless vortex shedding frequency f_{vs} versus dimensionless fiber length \hat{L} . f_{vs} increases with \hat{L} in the range of (0.18, 0.75). As already mentioned above, as \hat{L} increases, the effective \hat{K}_b decreases because of the greater effective incoming flow speed. Therefore f_{vs} increases with \hat{L} . The line $f_{vs} = 0.79\hat{L} + 0.73$ fits the data best in the sense of the least squares, which indicates the dimensionless vortex shedding frequency increases approximately linearly with the dimensionless fiber length.

Fig. 13 plots the critical Reynolds number Re_c versus dimensionless fiber length \hat{L} . It is seen that the Re_c increases with \hat{L} in the range of (0.18, 0.75). The line fitting the data by the least squares is $Re_c = 89\hat{L} + 28$. The data on Re_c has an error of ± 5 . A greater \hat{L} means a narrower flow channel which imposes a stricter constraint on the wake behind the fiber through its two rigid sidewalls. Therefore it becomes more difficult for the wake to oscillate. This may explain why Re_c is an increasing function of \hat{L} .

Basing on the group of simulations with varying dimensionless fiber length, we conclude that the fiber length \hat{L} has significant influence on vortex shedding and drag-coefficient. Re_c and f_{vs} both increase nearly linearly with the increase of \hat{L} . The averaged drag-coefficient \bar{C}_d increases with \hat{L} first and later becomes roughly constant.

IV. Summary and Discussion

Three sets of simulations have been designed and performed to investigate the influences of the Reynolds number, fiber dimensionless flexure modulus and dimensionless length on vortex shedding and drag-coefficient of the fiber. Our simulations have demonstrated the

discernable differences in shed vortices and the consequential fiber vibration and oscillation in drag-coefficient. According to these simulations, we conclude that, within the ranges of parameters used in our simulations, 1) The Reynolds number has significant influence on vortex shedding and fiber vibration. However, the Reynolds number has little influence on the averaged drag-coefficient \bar{C}_d for Re in $[200, 800]$. It appears that the $C_d - t$ curve becomes somewhat less oscillatory as Re increases. 2) The fiber dimensionless flexure modulus has significant influence on vortex shedding, fiber vibration and the $C_d - t$ curve. As \hat{K}_b increases, both the dimensionless vortex shedding frequency f_{vs} and the critical Reynolds number Re_c decrease approximately in the form of power laws. 3) The dimensionless fiber length has significant influence on vortex shedding, fiber vibration and the $C_d - t$ curve. Re_c and f_{vs} each increases linearly with \hat{L} . \bar{C}_d increases with \hat{L} first and becomes insensitive to \hat{L} later.

Williamson and Govardhan (2004) classified vortex shedding from an elastically mounted cylinder into three major patterns: the 2S mode (two single vortices per cycle), the 2P mode (two vortex pairs per cycle) and the P+S mode (a vortex pair and a single vortex per cycle). Our simulations show that vortex shedding from the flexible fiber with the mid-point tethered belongs to the 2S mode. Neither a 2P mode nor a P+S mode was found. Compared to the vortex shedding seen in the Fig. 2 of the paper by Alben et al. (2004), vortex shedding from our simulations appears different, especially in the wake away from the fiber. Perhaps this is because of the significant difference in Re which has important influence on vortex shedding, as illustrated in Fig. 2 of this paper. The vortex shedding reported here is similar to those observed from a flapping filament in Zhu (2001) and Zhu & Peskin (2002), from the two in-phase-flapping filaments in Zhu & Peskin (2003), and from a stationary rubber loop in Jung et al. (2006). But it is different from the vortex shedding from the two anti-phase-flapping

filaments in Zhu & Peskin (2003) (none of the above modes), from the flapping rubber loop in Jung et al. (2006) (2P mode), and from the side-by-side cylinders in Wang et al. (2005) (very complicated).

According to our simulations, it appears that the degree of oscillation in the $C_d - t$ curve lessens somewhat as Re increases while the fiber vibration range widens. In the laboratory experiment by Alben et al. (Re was between 2000 and 40,000), no oscillation in the drag or drag coefficient was found. Is the oscillation in drag-coefficient completely gone when Re becomes sufficiently high? This seems to be possible based on our simulations at lower Re . The current Navier-Stokes solver used in the IB method is not accurate for very high Re flows. At this point we cannot confirm this conjecture. However, this phenomenon seems to be counter-intuitive and may deserve further research.

According to our simulations at lower Re , the fiber-fluid problem becomes unsteady when vortex shedding occurs, and the fiber vibration range increases with Re . In the work by Alben et al. (2002, 2004) where the Re was significantly higher, the flow was steady and the fiber assumes a definite shape and position for a given set of flow parameters. The averaged shape and position of the fiber at the “quasi-steady” state in our simulation were compared in Fig. 14 with those (both experimental and numerical) reported in Fig.3 (a) of Alben et al. (2002) for three cases ($\eta = 6, 15, 20$)³ where the experimental and numerical results in Alben et al. (2002) agreed extremely well. It is seen that although the fiber shapes in our simulations were similar to those in Alben et al. (2002) obvious quantitative differences exist. Notice that the results in Alben et al. (2002) all sit above our averaged simulation results.

³The η is defined as $\sqrt{\frac{\rho_0 L^3 V_0^2 / 2}{Kb}}$ in Alben et al. (2002). It measures the relative importance of fluid kinetic energy and elastic potential energy. The relationship between η and \hat{K}_b is $\hat{K}_b = \frac{1}{2\eta^2}$.

The discrepancy between our results and Alben et al.’s may be explained by the fact that the Re in our simulations is lower by two orders of magnitude. (It appears that the higher the Re , the wider the opening of the fiber. See Fig. 3.) For more comparisons with Alben et al.’s work (e.g. drag), see Zhu & Peskin (2007).

Presumably the oscillation in the $C_d - t$ curve is caused by the vibration of the fiber which is induced by vortex shedding. It is expected that there exist functional relationships among the frequencies of oscillation in C_d , in fiber vibration and vortex shedding. However, the fiber vibration is more complicated than expected. Unlike the “simple” periodic up-and-down flapping with a single frequency of a flexible rod supported at the middle point, the flexible fiber vibrates in a more complicated fashion in the flowing fluid. Although not shown here, from an animation based on the simulation, it is seen that small-amplitude “irregular” vibrations occur almost everywhere on the whole fiber except near the tethered point. According to our simulations the vibration induced by vortex shedding is always small (in terms of amplitude compared to its length) and the lock-in phenomenon described in Williamson and Govardhan (2004) was not found. It seems that the small-amplitude vortex-shedding-induced vibration is “lost” in the background “noise” (the localized irregular motions). This makes the fiber motion difficult to quantify. Only the range of the fiber position is given in the paper. Fiber flexibility and interaction with the local fluid flowing by are supposed to be responsible for the complexity of fiber motion. Consequentially, FFT analysis performed on the $C_d - t$ data did not reveal any distinct frequencies for most of the cases. Only in a few cases a distinct frequency “happens” to exist. (It is not yet clear what is the underlying reason for this.) However, no quantitative relationship between the frequency and vortex shedding frequency was found neither for these cases. One such example is given below. Fig. 15 shows the results

for a simulation with a 3.3 *cm* fiber with bending modulus 2.8 *erg · cm* in a flowing fluid with kinematic viscosity 4 *cm²/s*. The inflow speed was 212.5 *cm/s*. (The dimensionless parameters are: $Re = 175$, $\hat{K}_b = 0.0065$, $\hat{L} = 0.3667$, $Fr = 14$, $\hat{K}_s = 5.369 \times 10^6$.) The left figure in Fig. 15 plots the positions of fluid markers at $T = 26$. The second one plots the vorticity contours at the same instant. The third one plots the $C_d - t$ curve. The last one plots the fiber shape and position with time. See the caption for details. Application of FFT on the $C_d - t$ data reveals a single distinct frequency, approximately 125, which is supposed to be the oscillation frequency in C_d . The vortex shedding frequency for this case was found to be 75.

Acknowledgement

The author would like to thank the unknown Referees for their suggestions and comments which have helped him for a better representation of his work. The author also thanks Silas Alben and Jun Zhang for providing their numerical and experimental data.

References

- [1] Abarbanel, S.S., Don, W.S., Gottlieb, D., Rudy D.H. & Townsend, J.C. 1991 Secondary frequencies in the wake of a circular cylinder with vortex shedding. *J. Fluid Mech.* **225**, 557.
- [2] Alben, S., Shelley, M. & Zhang, J. 2002 Drag reduction through self-similar bending of a flexible body. *Nature* **420**, 479.
- [3] Alben, S., Shelley, M. & Zhang, J. 2004 How flexibility induces streamlining in two-dimensional flow. *Physics of Fluids* **16**(5), 1694-1713.

- [4] Alben, S. 2004 Drag reduction by self-similar bending and a transition to forward flight by a symmetry breaking instability. *Ph.D thesis, Courant Institute of Mathematical Sciences, New York University.*
- [5] Bearman, P.W. 1989 Vortex shedding from oscillating bluff bodies. *Annu. Rev. Fluid Mech.* **16**, 195.
- [6] Griffin, O.M. & Ramberg, S.E. 1982 Some recent studies of vortex shedding with application to marine tubulars and risers. *Trans. ASME J. Energy Resour Technol.* **104**, 2.
- [7] Jung, S.W., Mareck, K., Shelley, M. & Zhang, J. 2006 Dynamics of a deformable body in a fast flowing soap film. *Phy. Rev. Lett.* **97** (13): Art. No. 134502.
- [8] Krasny, R. 1990 Vortex sheet roll-up due to the motion of a flat plate. *FED-Vol. 92, International Symposium on nonsteady fluid dynamics*, Editors: J.A. Miller, and D.P. Telionis, Book No. H00597 - 1990.
- [9] Lee, S. 2000 A numerical study of the unsteady wake behind a sphere in a uniform flow at moderate Reynolds numbers. *Computers & Fluids* **29**, 639.
- [10] Nitsche, M. & Krasny, R. 1994 A numerical study of vortex ring formation at the edge of a circular tube, *J. Fluid Mech.* **276**, 139.
- [11] Parkinson, G.V. 1989 Phenomena and modelling of flow-induced vibrations of bluff bodies. *Prog. Aerosp. Sci.* **26**, 169.

- [12] Peskin, C.S. 1977 Flow patterns around heart valves: a numerical method. *J. Comp. Phys.* **25**, 220.
- [13] Peskin, C.S. & McQueen, D.M. 1996 Fluid dynamics of the heart and its valves. in *Case Studies in Mathematical Modeling: Ecology, Physiology, and Cell Biology*, edited by H.G. Othmer, F.R. Adler, M.A. Lewis, and J.C. Dallon, p.309 (Prentice-Hall, Englewood Cliffs, NJ, 1996).
- [14] Peskin, C.S. 2002 The immersed boundary method. *Acta Numerica* **11**, 479.
- [15] Sarpkaya, T. 1975 An inviscid model of two-dimensional vortex shedding for transient and asymptotically steady separated flow over an inclined flat plate, *J. Fluid Mech.* **68**, 109.
- [16] Sarpkaya, T. 1979 Vortex-induced oscillations. *ASME J. Appl. Mach.* **46**, 241.
- [17] Wang, Z.J. & Zhou, Y. 2005 Vortex interactions in a two side-by-side cylinder near-wake. *Int. J. Heat and Fluid Flow* **26**, 362.
- [18] Williamson, C.H.K. & Govardhan, R. 2004 Vortex-induced vibrations. *Annu. Rev. Fluid Mech.* **36**, 413.
- [19] Zhu, L. 2001 Simulation of a flapping flexible filament in a flowing soap film by the immersed boundary method. *Ph.D thesis, Courant Institute of Mathematical Sciences, New York University.*
- [20] Zhu, L. & Peskin, C.S. 2002 Simulation of a flapping flexible filament in a flowing soap film by the immersed boundary method. *J. Comp. Phys.* **179**, 452.

- [21] Zhu, L. & Peskin, C.S. 2003 Interaction of two flapping filaments in a flowing soap film. *Phys. of Fluids* **15**, no. 7.
- [22] Zhu, L. & Peskin, C.S. 2007 Drag of a flexible fiber in a 2D moving viscous fluid. *Computers & Fluids*, **36**, 398-406.

A typical initial velocity profile

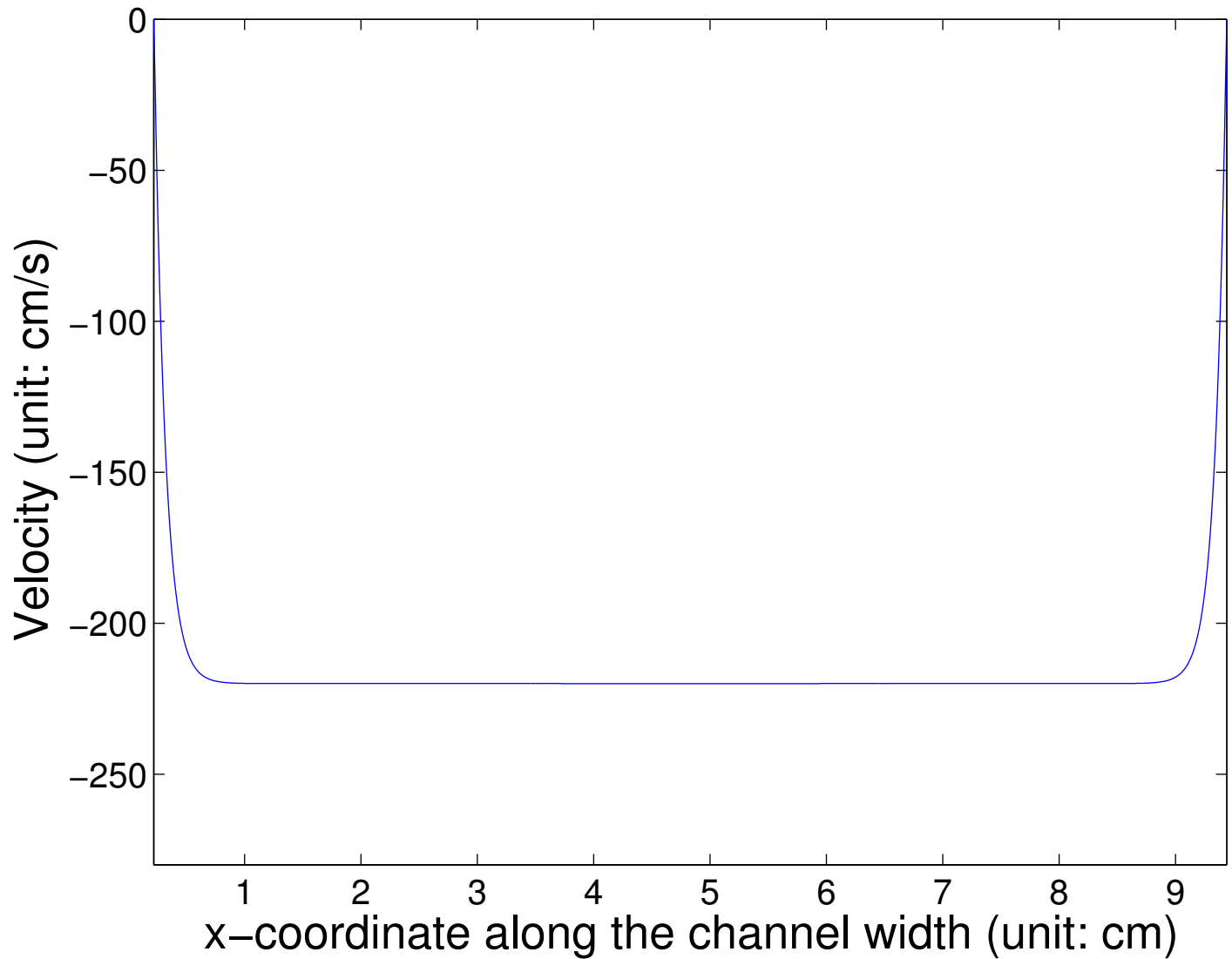


Figure 1: The initial velocity and inflow velocity profiles for inflow speed 220 cm/s . The x-axis represents the flow tunnel width direction. The y-axis is the 2^{nd} component (i.e. $v(x)$) of the velocity $\mathbf{u}(\mathbf{x}, 0)$. (Note v is a function of x only here and the 1^{st} velocity component is zero.) Note that the inflow velocity profile is a flat line on most part of the channel except near the left and right boundaries; this is because of the air resistance. This profile is imposed as the initial condition and inlet/outlet boundary conditions for velocity.

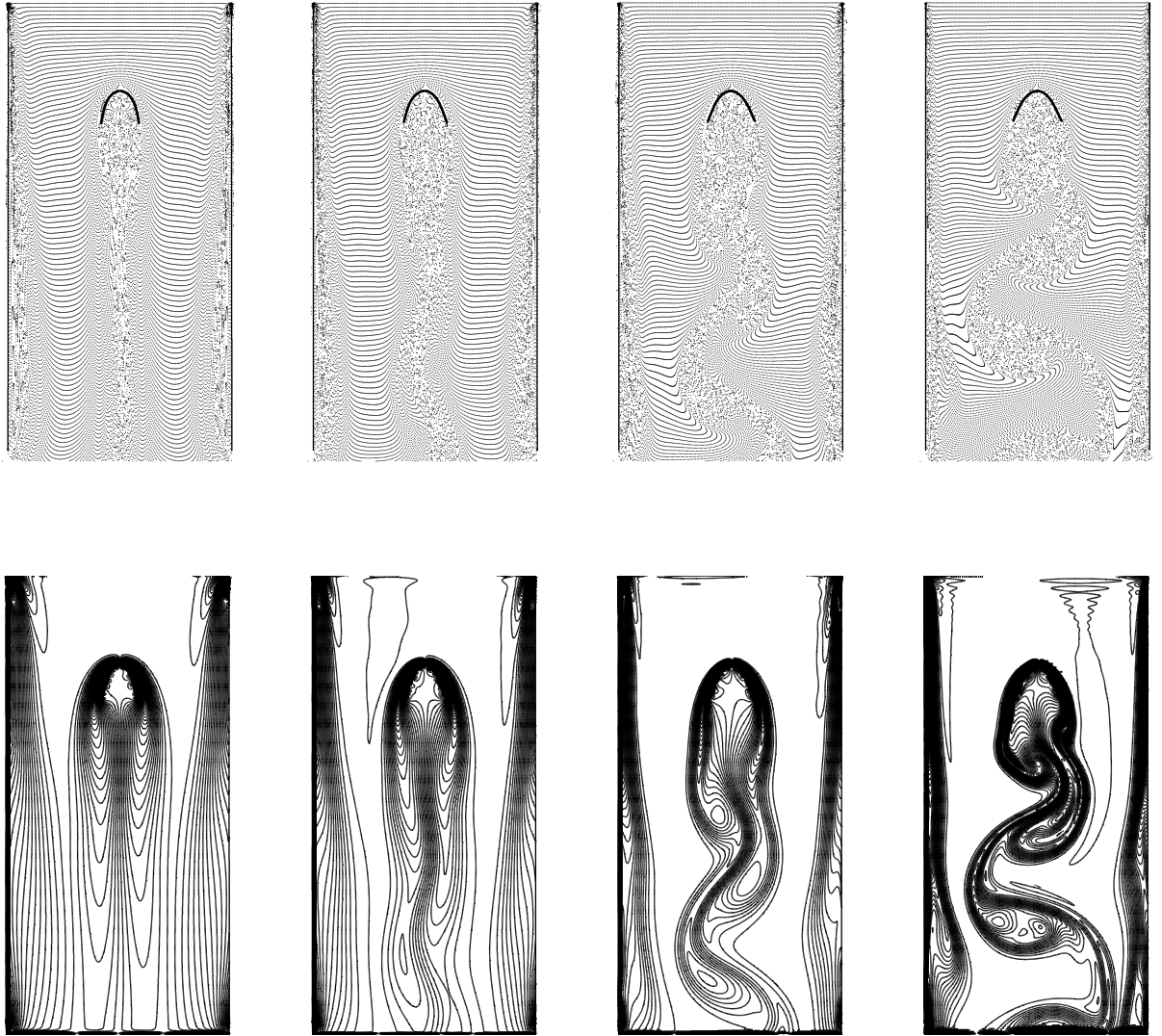


Figure 2: Visualization of the flow and vortical field at four different Reynolds numbers at dimensionless time 24. The upper panel is the instantaneous positions of fluid markers at four different instants and the lower panel is the vorticity contours at corresponding time. The Reynolds number is 82.5, 165, 330, 660, from left to right respectively.

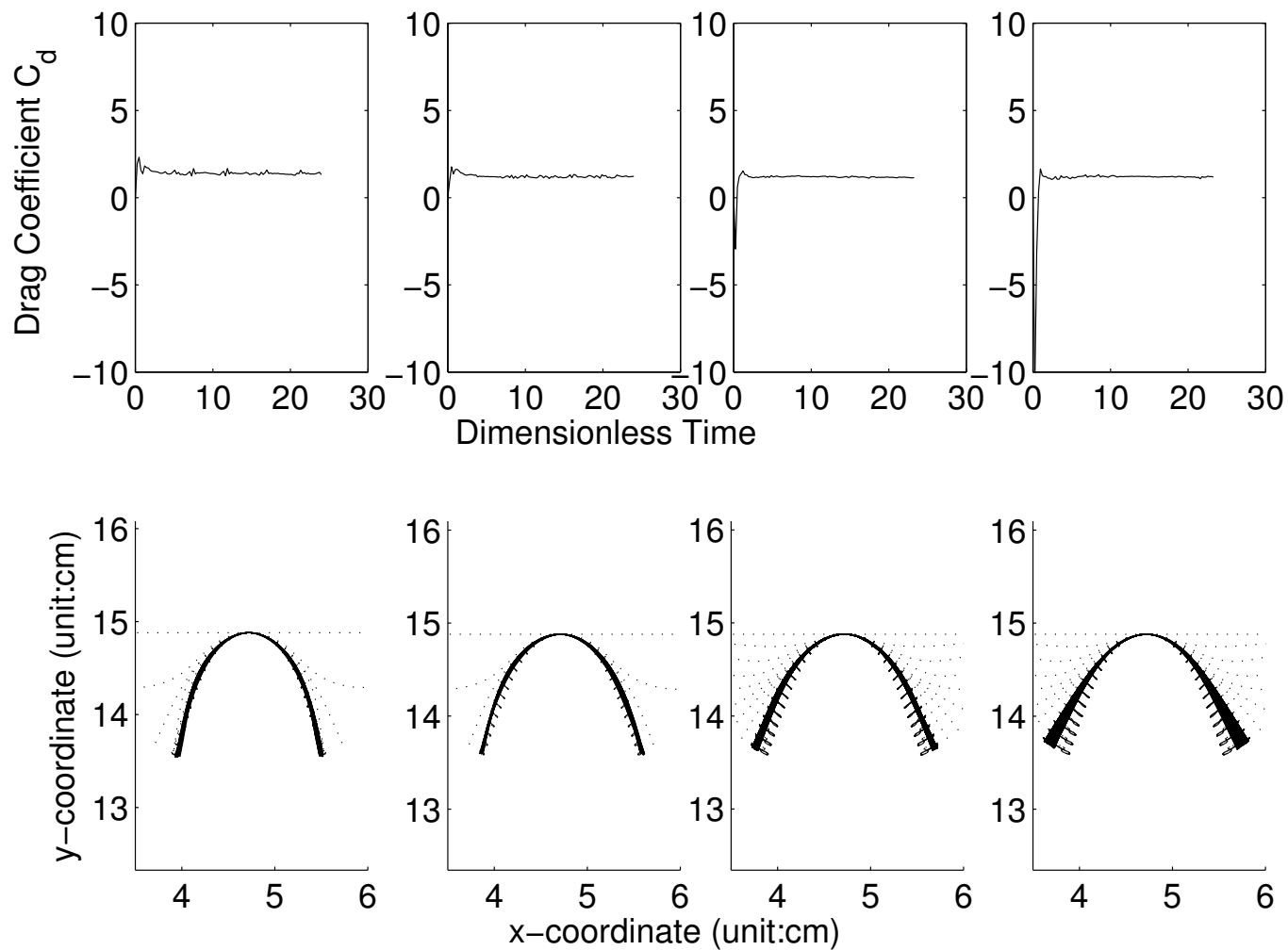


Figure 3: The drag-coefficient versus dimensionless time and position of the fiber at four different Reynolds numbers. The upper panel plots the drag-coefficient as a function of time and the lower panel plots the corresponding position of the fiber. The dotted and solid lines are the fiber positions before and after it reaches the “quasi-steady” state, respectively. The thickness of the solid lines (many lines overlap) represents the fiber oscillation range. The Reynolds number Re is 82.5, 165, 330, 660, from left to right respectively.

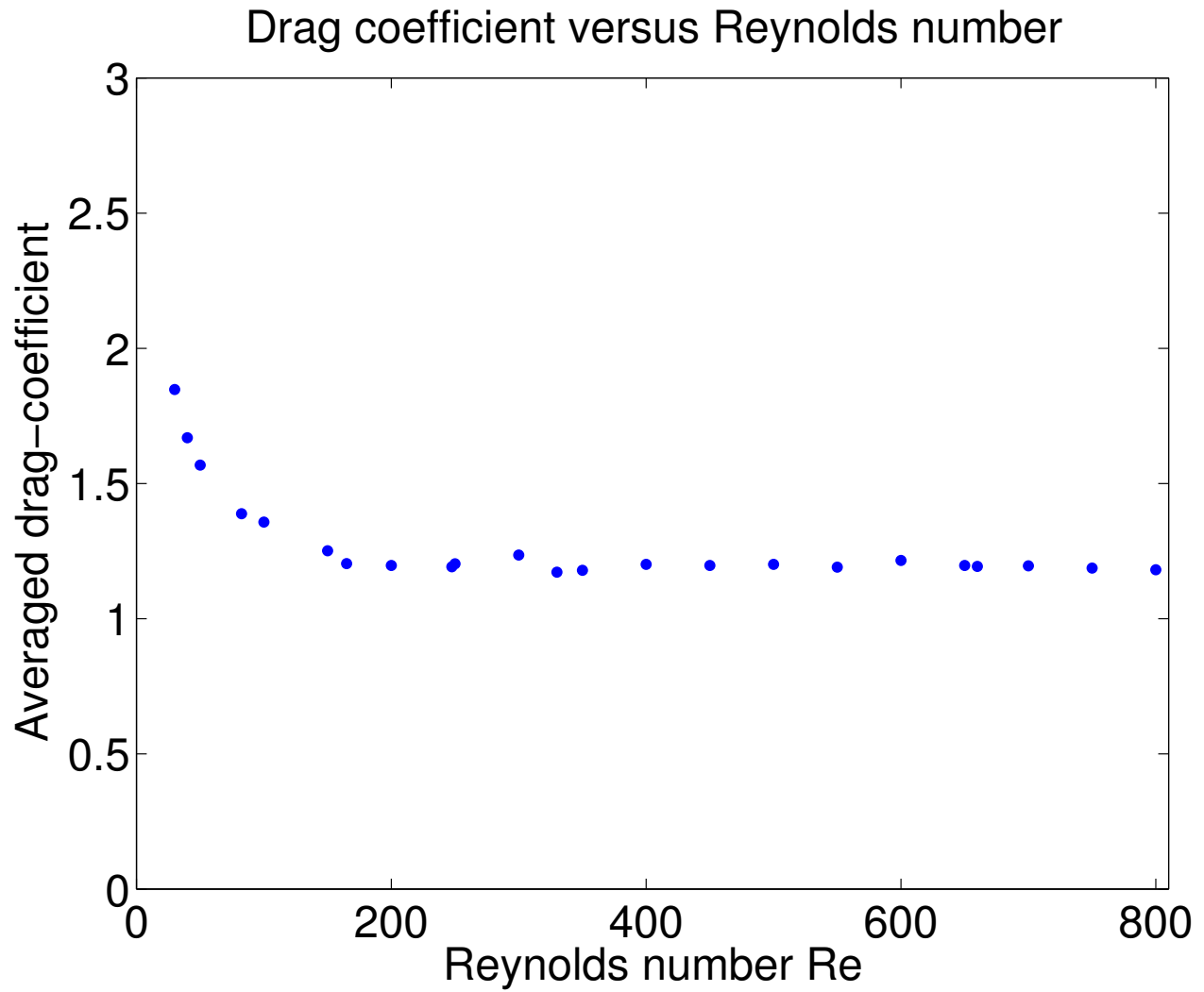


Figure 4: Averaged drag coefficient \bar{C}_d versus Reynolds number Re . The drag-coefficient varies very slowly with Reynolds number (\bar{C}_d is nearly a constant) for Re between 200 and 800, and increases rapidly when Re gets smaller.

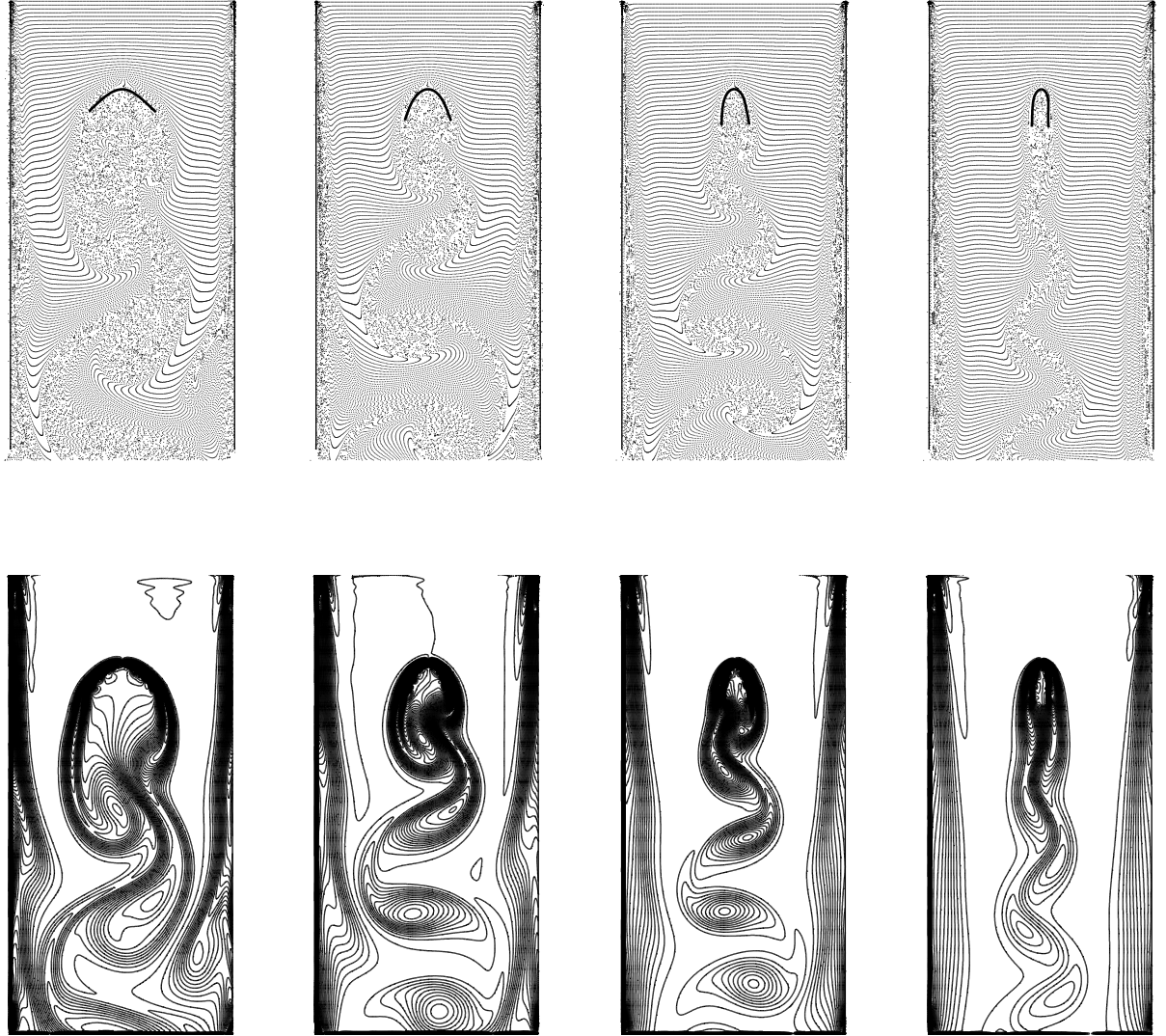


Figure 5: Visualization of the flow and vortical field at dimensionless time 30. The upper panel is the instantaneous positions of fluid markers and the lower panel is the vorticity contours. The value of K_b is 2.89×10^{-2} , 7.21×10^{-3} , 1.44×10^{-3} , and 2.89×10^{-4} , from left to right respectively.

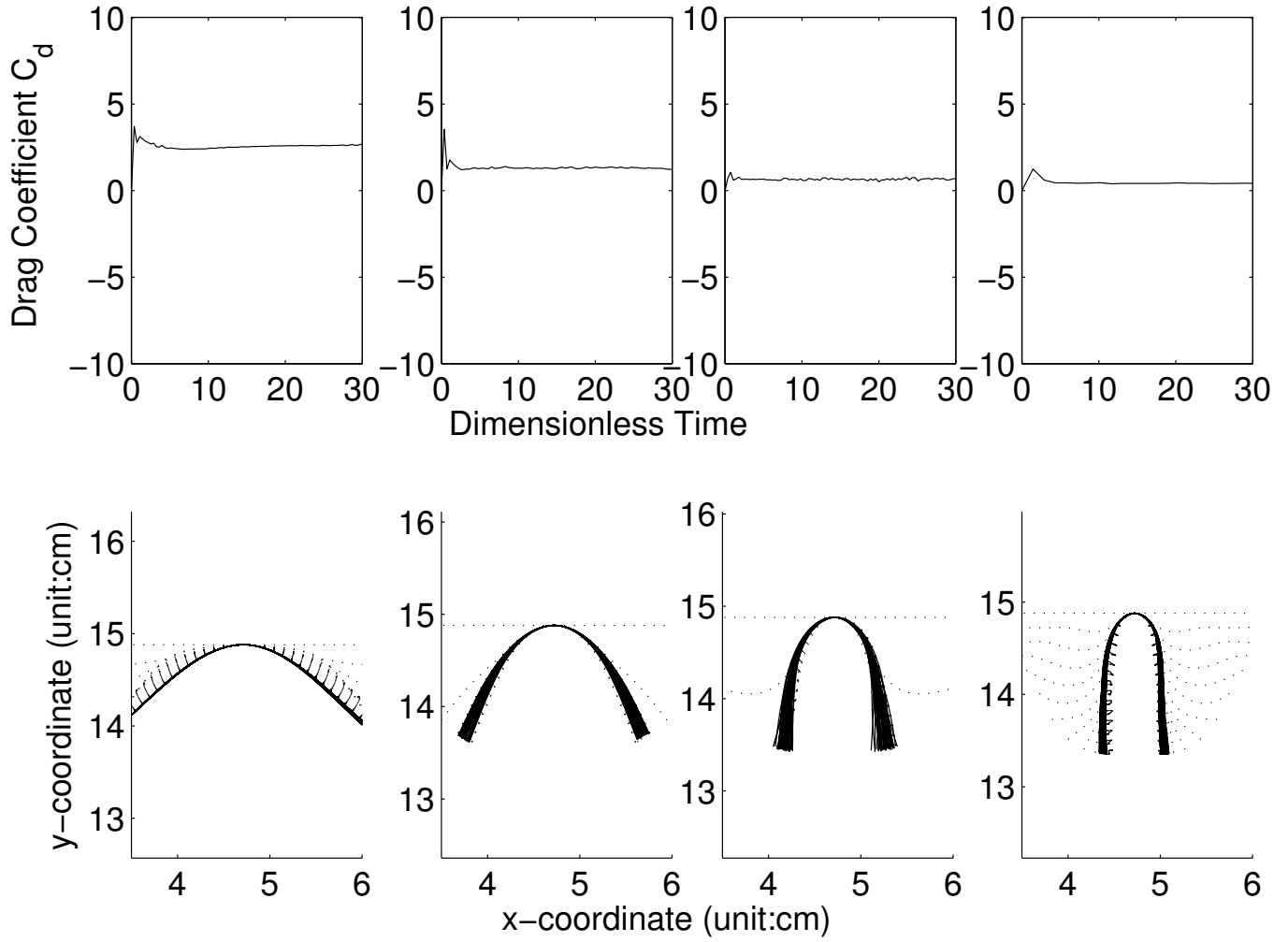


Figure 6: The drag-coefficient and position of the fiber at four different values of the dimensionless bending rigidity \hat{K}_b . The upper panel plots the drag-coefficient as a function of time and the lower panel plots the corresponding position of the fiber. The dotted and solid lines are the fiber positions before and after it reaches the “quasi-steady” state, respectively. The thickness of the solid lines (many lines overlap) represents the fiber oscillation range. The value of \hat{K}_b is 2.89×10^{-2} , 7.21×10^{-3} , 1.44×10^{-3} , and 2.89×10^{-4} , from left to right respectively.

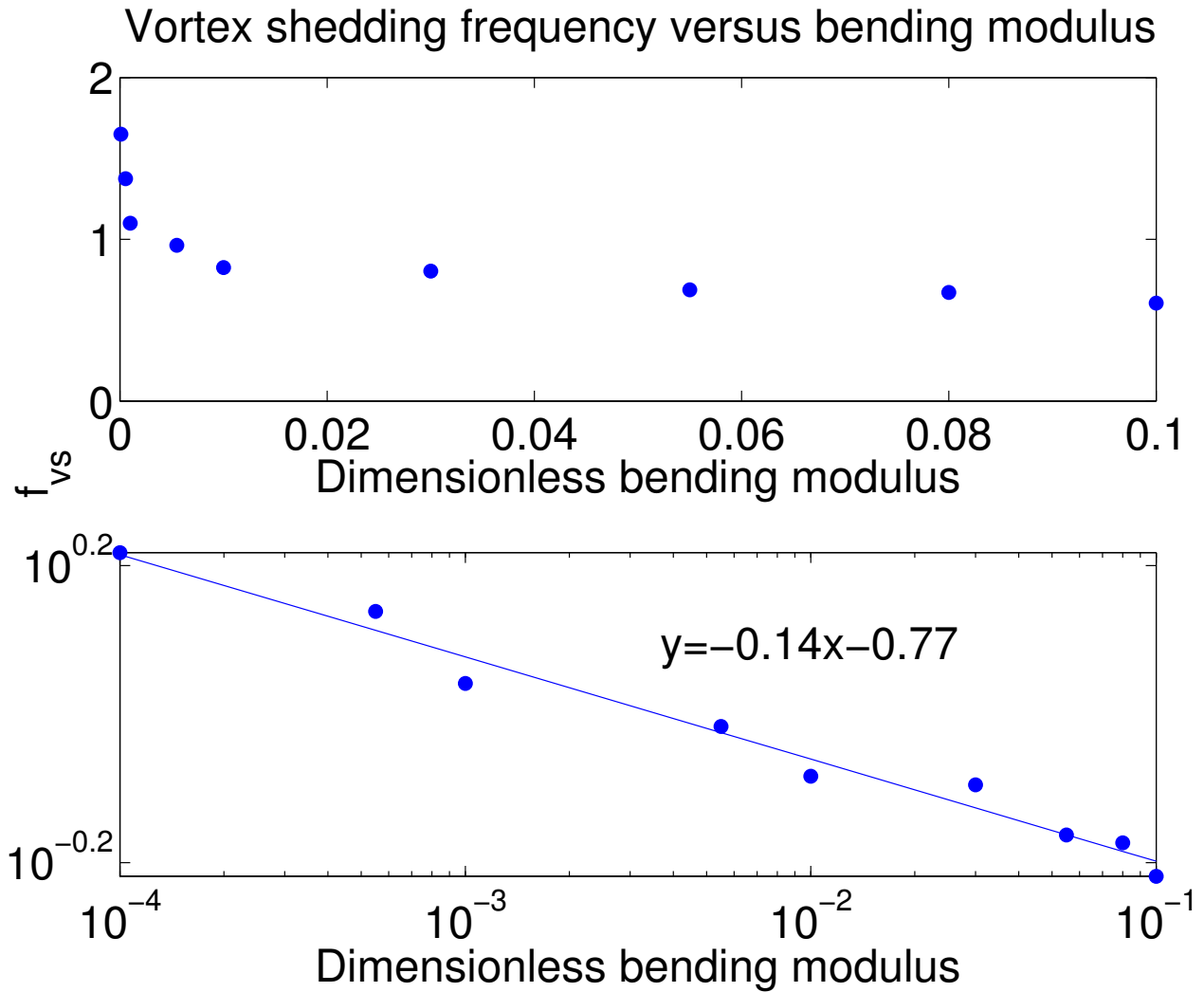


Figure 7: Dimensionless vortex shedding frequency f_{vs} versus dimensionless bending modulus \hat{K}_b . The x-axis is the bending modulus and the y-axis is the shedding frequency. The top figure plots f_{vs} as a function of \hat{K}_b . The bottom one is a log-log plot of the data. The line $y = -0.14x - 0.77$ fits the data best in the least squares sense. This shows the f_{vs} decreases approximately as $\hat{K}_b^{-0.14}$ which is valid for \hat{K}_b in $(10^{-4}, 10^{-1})$.

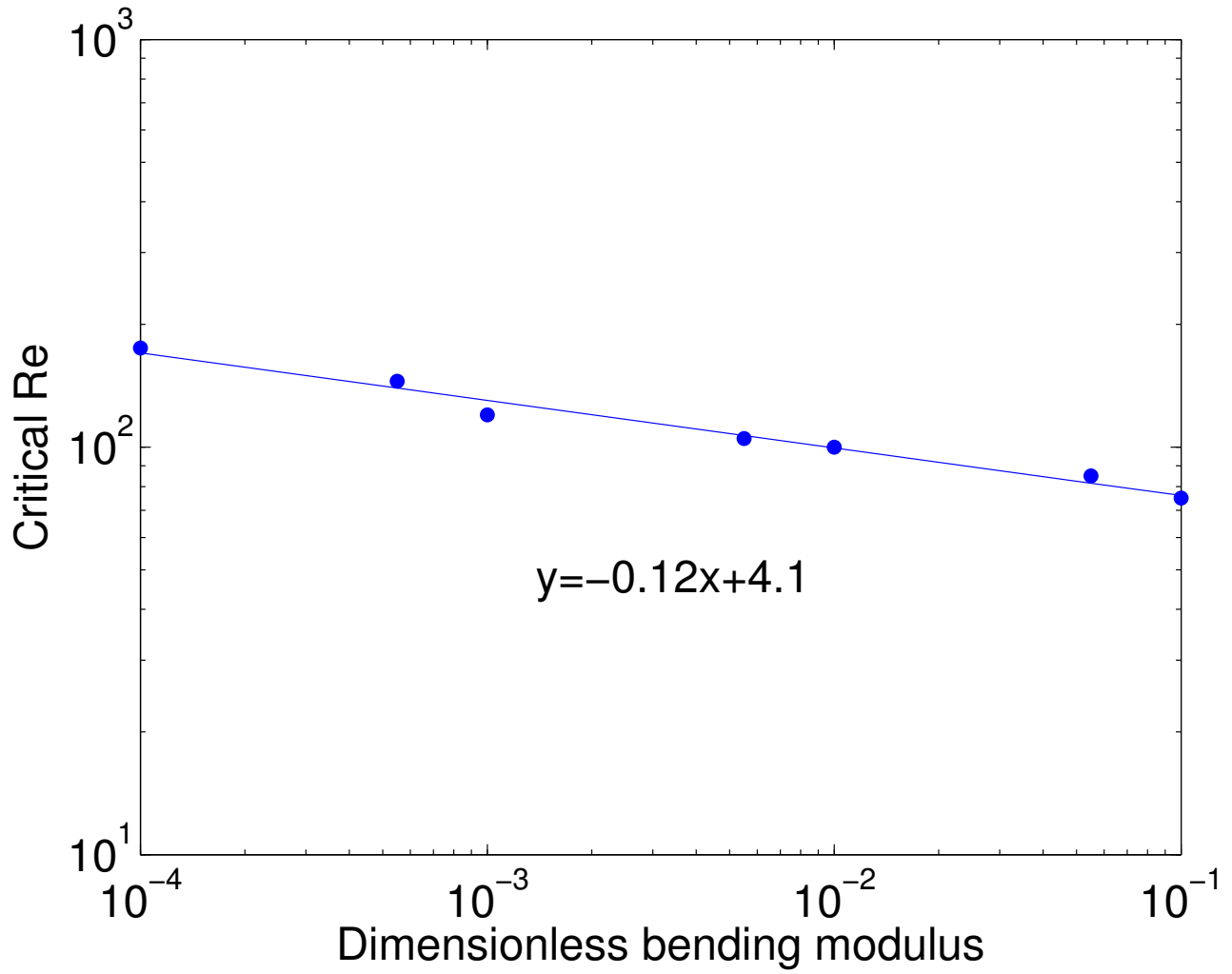


Figure 8: A log-log plot of critical Reynolds number Re_c for vortex shedding versus dimensionless bending modulus \hat{K}_b . The x-axis is the bending modulus and the y-axis is the critical Reynolds number. The critical Reynolds number decreases as the dimensionless bending modulus increases. The best fitting line by the least squares is $y = -0.11x + 4.1$. The data of Re_c contains an error of ± 5 .

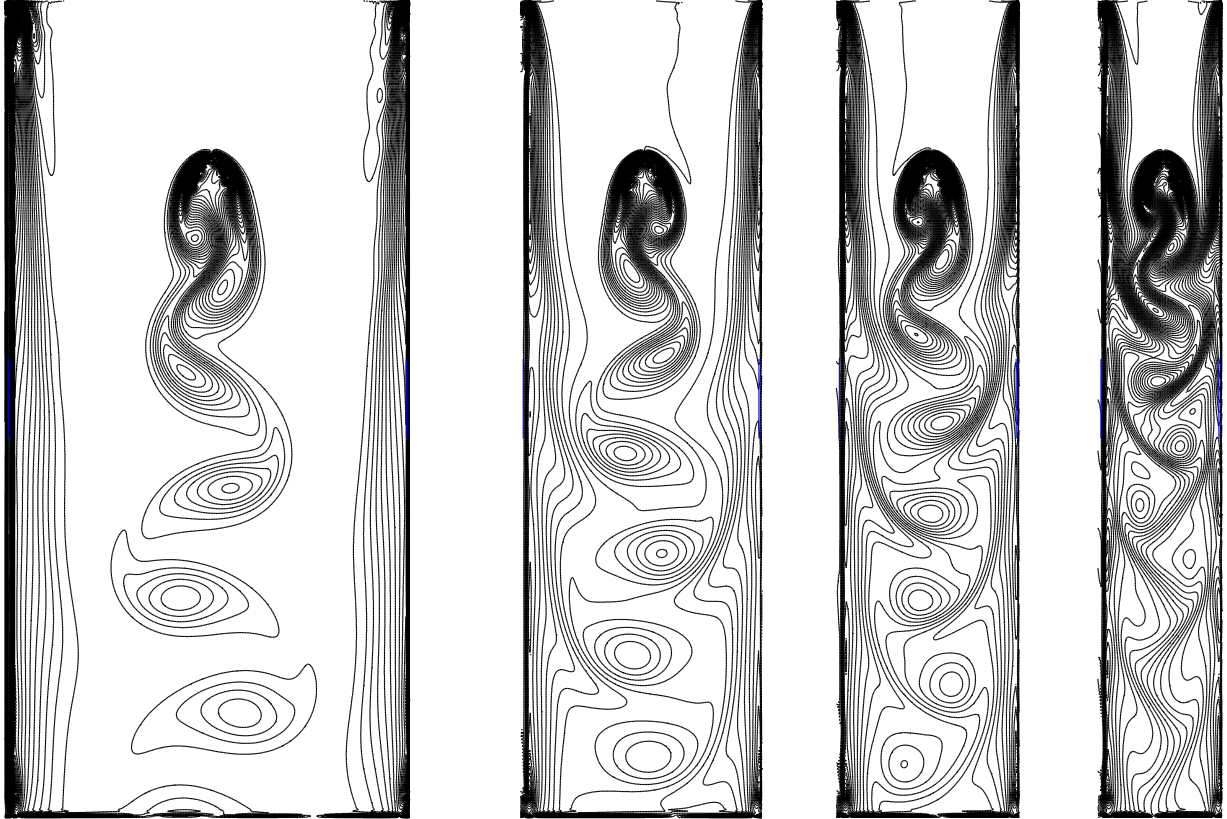


Figure 9: Visualization of vortical field. The figure plots the vorticity contours for 4 different dimensionless fiber length \hat{L} at dimensionless time 30. The four values of \hat{L} are 0.1778, 0.4, 0.6, 0.8, from left to right respectively.

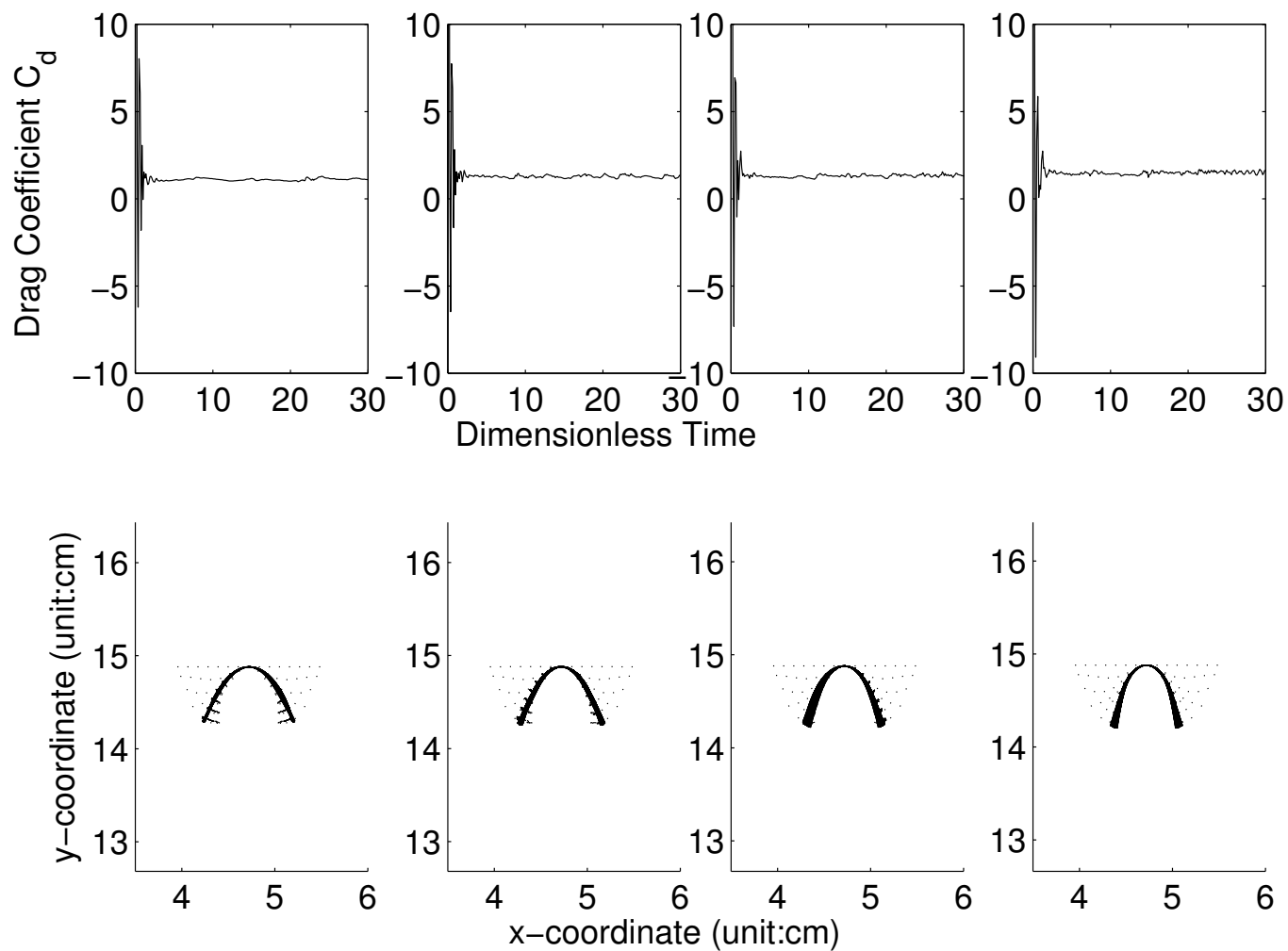


Figure 10: The drag-coefficient and position of the fiber at four different values of fiber length. The upper panel plots the drag as a function of time and the lower panel plots the corresponding position of the fiber. The dotted and solid lines are the fiber positions before and after it reaches the “quasi-steady” state, respectively. The thickness of the solid lines (many lines overlap) represents the fiber oscillation range. The value of \hat{L} is 0.1778, 0.4, 0.6, 0.8, from left to right respectively.

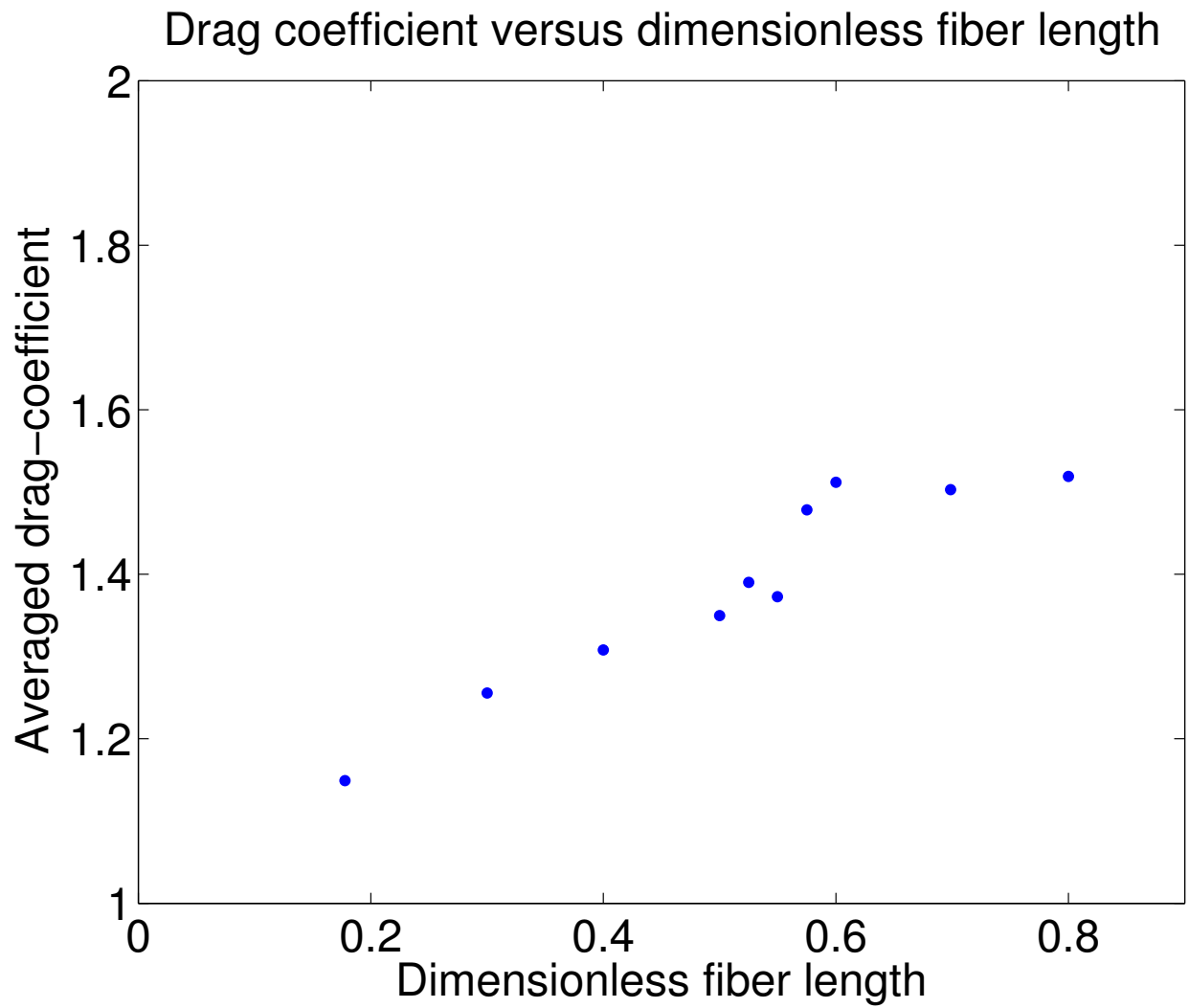


Figure 11: The averaged drag coefficient \bar{C}_d versus dimensionless fiber length \hat{L} .

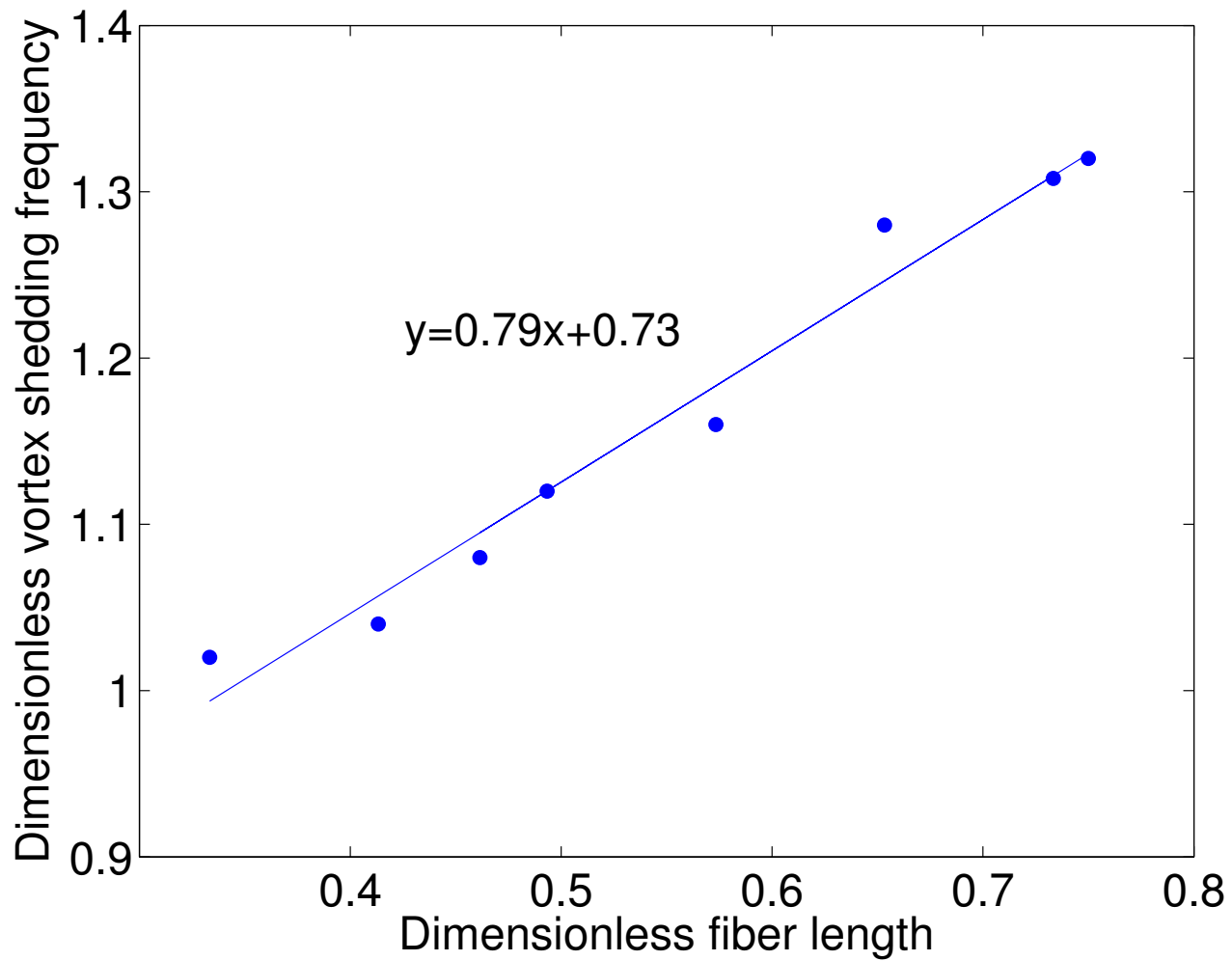


Figure 12: Dimensionless vortex shedding frequency f_{vs} versus dimensionless fiber length \hat{L} . The x-axis is the fiber length and the y-axis is the shedding frequency. The data shows f_{vs} increases as \hat{L} increases. The line fitting the data best in the least squares sense is $y = 0.79x + 0.73$.

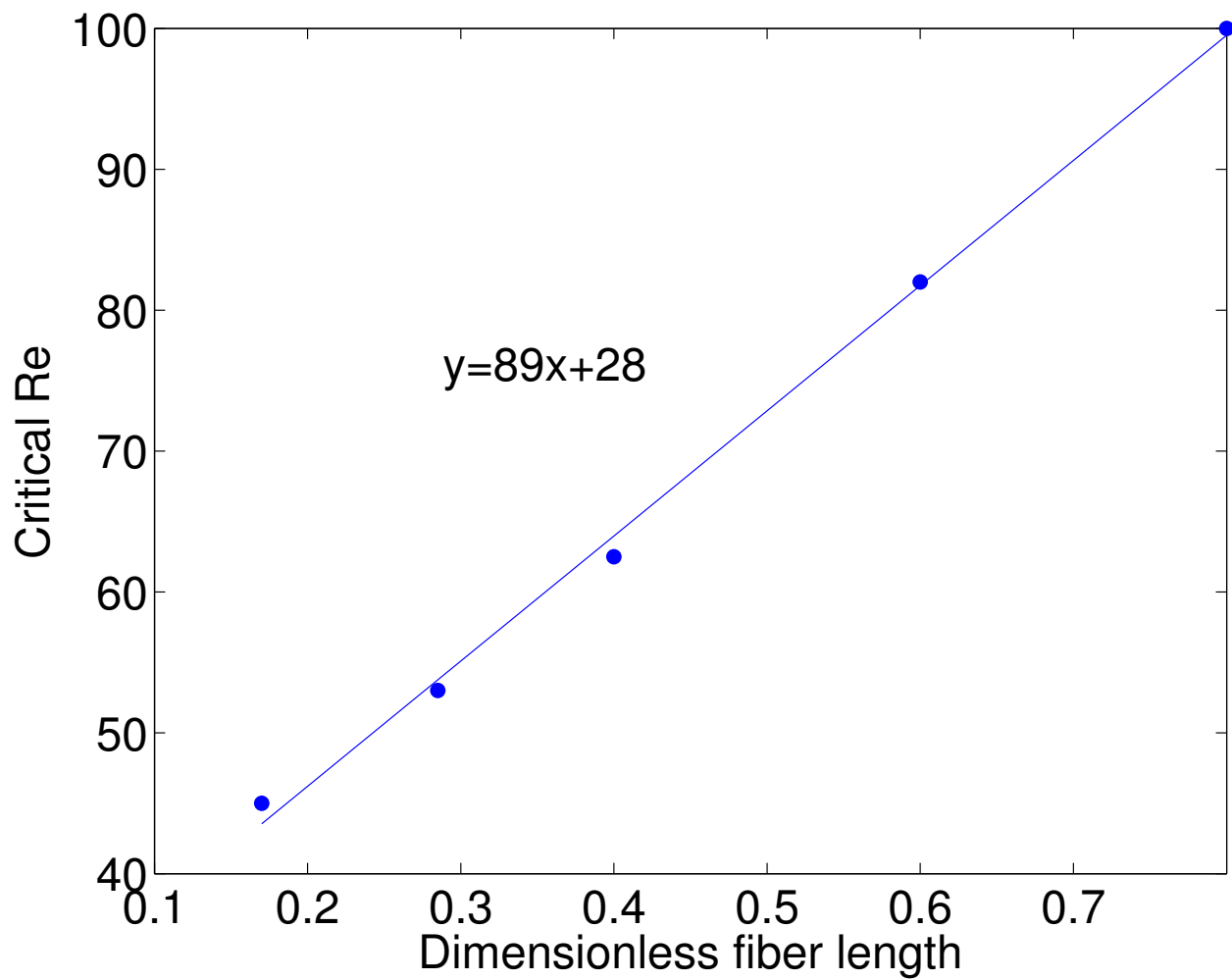


Figure 13: Critical Reynolds number Re_c versus dimensionless fiber length \hat{L} . The x-axis is the fiber length and the y-axis is the critical Reynolds number. The Re_c increases as \hat{L} increases. The best fitting line by the least squares is $y = 89x + 28$.

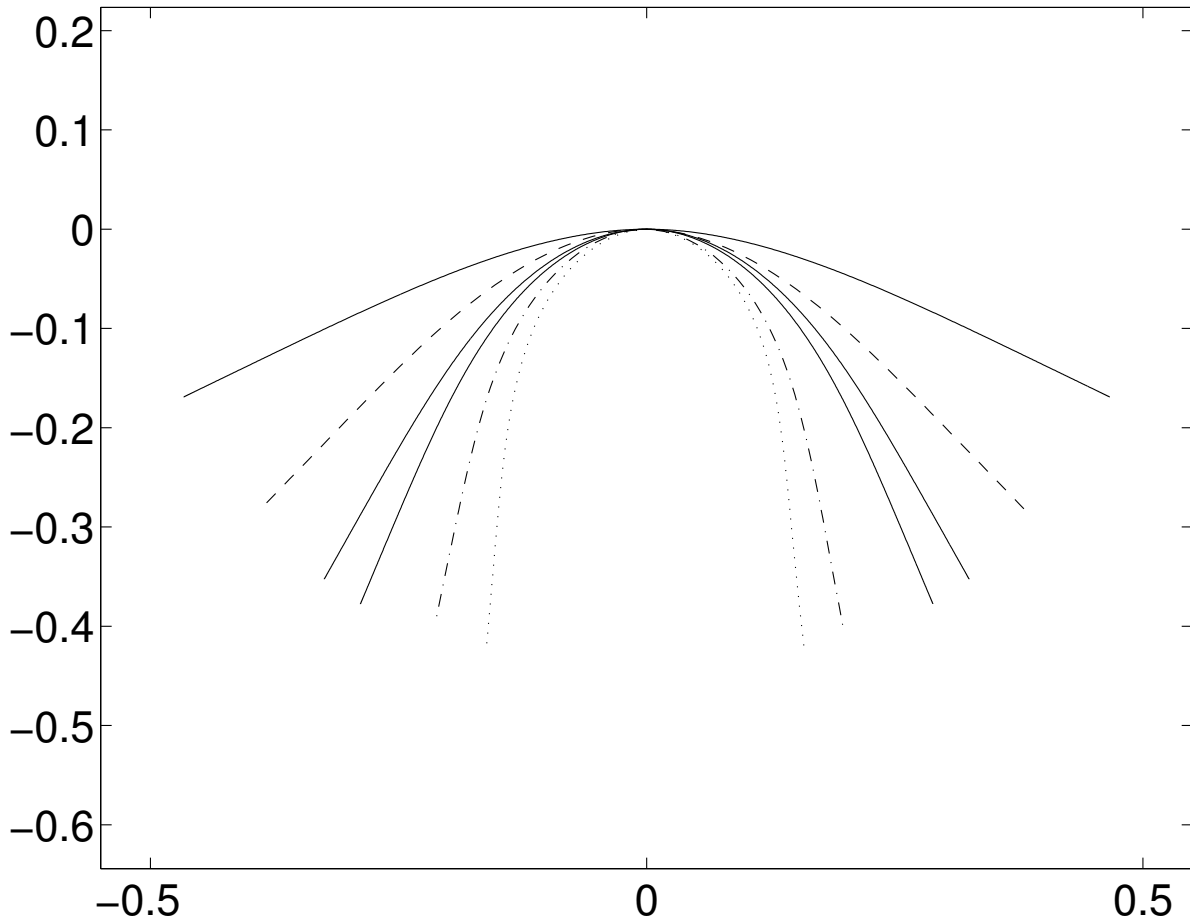


Figure 14: Comparison of averaged fiber shapes from our simulations with those in the work of Alben et al. (2002). The x and y coordinates are nondimensionalized by the fiber length (1.95 cm). The three solid lines are results from Alben et al. (2002). The values of η for the solid lines are 5, 12, 20 from top to bottom, respectively. Note that the experimental results and numerical results in Alben et al. (2002) are almost not distinguishable for the three values of η and only the numerical results are shown here. The other three lines are our simulation results. The value for η is 5 for the dashed line, 12 for the dashdotted line, and 20 for the dotted line. The relation between η and \hat{K}_b is $\hat{K}_b = \frac{1}{2\eta^2}$. The Reynolds number for the three simulations is 600 which is approximately 100 times less than the experimental value. This may explain the quantitative differences shown in the figure. Notice that each curve from Alben et al. lies above the corresponding curve from our simulation. See the bottom panel of Fig. 2 for the influence of Re on fiber shape.

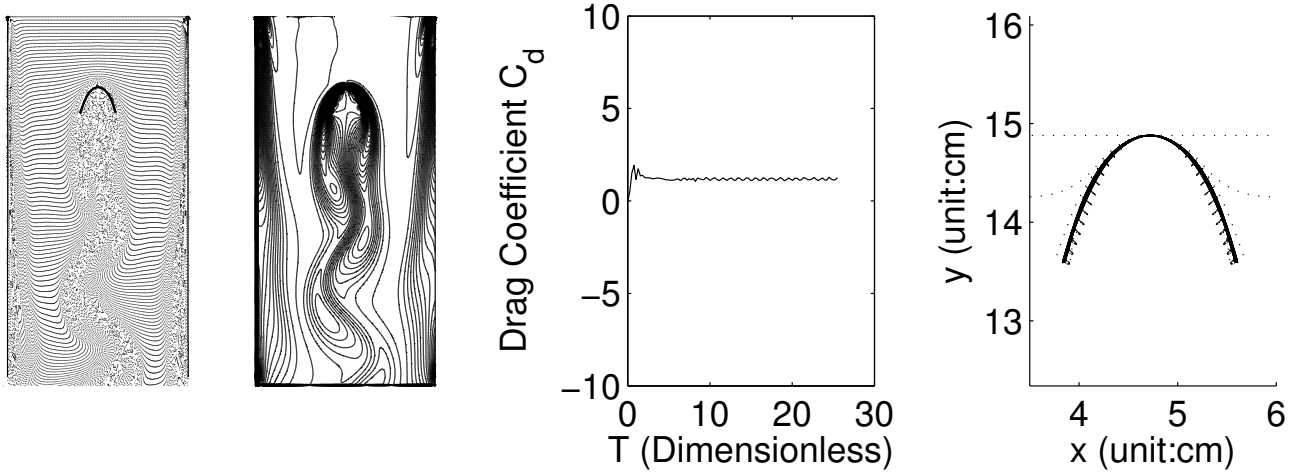


Figure 15: The simulation results where the FFT analysis on $C_d - t$ data reveals a single distinct frequency. The parameters used for this simulation were $L = 3.3 \text{ cm}$, $K_b = 2.8 \text{ erg} \cdot \text{cm}$, $\nu = 4 \text{ cm}^2/\text{s}$, $V_0 = 212.5 \text{ cm/s}$. (The dimensionless parameters are: $Re = 175$, $\hat{K}_b = 0.0065$, $\hat{L} = 0.3667$, $Fr = 14$, $\hat{K}_s = 5.369 \times 10^6$.) The first figure from left is the positions of fluid markers. The second one is the vorticity contours. The third one plots the drag-coefficient versus time. The last one plots the positions of the fiber. The oscillation in $C_d - t$ has a distinct frequency of 125 Hz. The vortex shedding frequency is 75 Hz.